DR QI AN (Orcid ID : 0000-0003-4838-6232)

Article type : Special Issue Article

Strengthening Boron Carbide by Doping Si into Grain Boundaries

Yidi Shen,[1] Moon Young Yang[2], William A. Goddard III[2*] and Qi An[1*]

1 Department of Chemical and Materials Engineering, University of Nevada, Reno, Reno, Nevada, 89577, United States

2 Materials and Process Simulation Center, California Institute of Technology, Pasadena, CA 91125, United States

Correspondence Author Emails: wag@caltech.edu ; qia@unr.edu

Abstract

Grain boundaries, ubiquitous in real materials, play an important role in the mechanical properties of ceramics. Using boron carbide as a typical superhard but brittle material under hypervelocity impact, we report atomistic reactive molecular dynamics simulations using the ReaxFF reactive force field fitted to quantum mechanics to examine grain boundary engineering strategies aimed at improving the mechanical properties. In particular, we examine the dynamical mechanical response of two grain boundary models with or without doped Si as a function of finite shear deformation. Our simulations show that doping Si into the grain boundary significantly increases the shear strength and stress threshold for amorphization and failure for both grain boundary structures. These results provide validation of our suggestions that Si doping provides a promising approach to mitigate amorphous band formation and failure in superhard boron carbide.

This article has been accepted for publication and undergone full peer review but has not been through the copyediting, typesetting, pagination and proofreading process, which may lead to differences between this version and the Version of Record. Please cite this article as doi: 10.1111/JACE.18028

1. INTRODUCTION

Boron carbide (B_4C) is a superhard material with a wide range of engineering applications, including personal body armor, abrasives, neutron capture materials[1], and high-pressure nozzles[2] because of its high hardness, low density, chemical inertness, resistance to wear, and high neutron absorption cross section.[3, 4] However, applications are limited by the brittle failure observed under hypervelocity impact or high pressure.[4, 5] Recent transmission electron microscopy (TEM) experiments indicated that this abnormal brittle failure arises from the formation of a very tiny amorphous shear band of 2~3 nm in width and 100~300 nm in length under various loading conditions of hypervelocity impact[5], indentation[6], laser shock[7], radiation[8], and mechanical scratching[9]. In order to explain the amorphization in B_4C, numerous theoretical studies focused on the atomic structural failure that leads to the amorphous shear bands. For instance, our previous DFT study showed that the structural failure of B_4C along the lowest shear stress slip system, $(01\bar{1}\bar{1})/[\bar{1}101]$ (or $(100)_r[001]_r$, using Rhombohedral lattice index) arises from the breaking first B-C bond connecting two icosahedra with the negative C reacting with the middle positive boron atom in the C-B-C chain.[10] This reaction causes the deconstruction of the icosahedra containing the C, which then contracts 5-10 % to higher density. Then to further determine how this amorphous band is related to brittle failure, reactive molecular dynamics (RMD) simulations were performed on finite shear deformations of B_4C with a large (25 nm × 25 nm) system of ~200,000 atoms.[11] Indeed, amorphous shear bands with a width of 2–3 nm were observed that led to twinning, followed by amorphization, cavitation, and finally crack formation.[11] The origin of the brittle failure is that deconstruction of the icosahedra increases the density by 5%, leading to tension and cavitation. Therefore, to prevent brittle failure in B_4C, we need to mitigate amorphous shear band formation.

Our QM studies showed that replacing the CBC chains with two-atom chains such as Si_2 and P_2 leads to ductile single crystals. This suggests that adding Si or P to the grain boundaries might improve ductility. Several approaches, such as microalloying[12–16], stoichiometry control[17–19], and addition of a 2nd phase[20–22], have been proposed to mitigate amorphous shear band formation. For microalloying, both non-metal dopants (P[23] and Si[24]), as well as metal dopants (Li[14, 15], Mg[12,16], and Ti[13]) may decrease amorphization in B_4C. Both experimental and theoretical studies have suggested

that boron enrichment is helpful to mitigate amorphization.[17–19] Moreover, the addition of the 2nd phase, such as SiC[25] and TiB_2[26] has been shown to improve the fracture toughness of B_4C.

Among these approaches, grain boundary (GB) engineering is promising. Boron carbide has sharp clean GBs,[22, 27] but the presence of GBs in boron carbide weakens the strength of icosahedra next to the GB, leading to amorphization and GB sliding in nanocrystalline B_4C.[28] Thus, to improve the fracture toughness of boron carbide it is important to mitigate amorphization initiated from GBs by proper design of the GBs. Previously ReaxFF RMD simulations and TEM observations were combined to examine the atomic level deformation mechanisms of nanocrystalline boron carbide (n-B_4C) with a range of grain sizes.[29] The results showed that high-energy GBs in n-B_4C promote GB sliding, resulting in higher ductility. Another approach for GB engineering is doping additives into the GBs.[30] Previous experiments demonstrated that Al and Si can be absorbed by the GBs in boron carbide to modify the GB chemistry.[31, 32] Moreover, a very recent experiment indicates that a small amount of Si (~1 at%) doped into boron carbide leads to short, diffuse and multivariant shear faults that arise from direct fragmentation to contribute to quasi-plasticity in Si-doped boron carbide.[33] This suggests that doping Si into boron carbide can markedly mitigate amorphous shear band formation, making Si a possible promising candidate for improving the mechanical properties of boron carbide through GB engineering.

In the present study, ReaxFF RMD simulations were performed to illustrate this Si doping GB engineering strategy to mitigate the amorphous band formation in B_4C. Our simulations find that boron enrichment mitigates amorphous shear band formation. More interesting, doping Si into the GB region significantly increases the critical stress for amorphization to strengthen polycrystalline boron carbide. Our results explain previous experimental findings that Si doping can mitigate the amorphization in boron carbide by fragmentation rather than amorphization.[33]

2. METHODOLOGY

2.1 ReaxFF simulations

All RMD simulations were performed using the ReaxFF reactive force field incorporated into the large-scale atomic/molecular massively parallel simulator (LAMMPS)[34]. The time step for integrating

the equation of motion was set to 0.5 fs. The periodic boundary conditions were applied to eliminate the surface effects. The NPT ensemble and NVE ensemble were applied in the RMD simulations.

For structural optimization, both atomic positions and cell parameters were allowed to relax to minimize potential energy. Using the optimized structure, the unit cell was rotated to make the "a axis" along the slip direction and the "c axis" along the slip plane. Then a supercell was constructed by expanding the rotated structure along all three directions. Next, the structure was relaxed at room temperature using the NPT ensemble for 10 ps. Finally, finite shear deformation was applied to examine shear-induced failure.

In order to control shear deformation, we considered three regions of the supercell: an immobile lower region with a thickness ~1 nm, an immobile upper region with a thickness ~1 nm, and a mobile region of ~5 nm between the immobile layers, as shown in Fig. S1 of Supplementary Materials (SM).[35] Then a velocity of 1×10^3 m/sec was assigned to the atoms in the upper layer while the atoms in the lower layer remained fixed. The atoms in the mobile layer were assigned velocities that initially varied from 0 to 1×10^3 m/sec on top of their thermal velocities at 300 K. The corresponding engineering strain rate for all simulations is $\sim 1 \times 10^{-3}$ ps^{-1}. We applied the NVE ensemble to describe the shear deformation for the mobile atoms while temperature control was achieved by velocity rescaling in the other two non-sheared directions.

For Si-doped GBs, we added 32 and 8 Si atoms in GB regions to retain the same doping concentration of ~0.09 at%. In addition, all the Si dopants were placed into the void sites in the GB regions and the void sites are close to GB atoms with larger atomic volume determined using Voronoi polyhedra.

2.2 Quantum simulations

QM simulations were performed to build the trainset for retraining ReaxFF to describe B-C systems. All QM calculations were performed using VASP package[34,35] with the Perdew-Burke-Ernzerhof (PBE) flavor of the generalized gradient approximation (GGA).[36,37] The $2s^2 2p^2$ electrons were described explicitly for C, $2s^2 2p^1$ electrons for B, and $3s^2 3p^2$ electrons for Si. The pseudopotentials were constructed using the projector augmented-wave (PAW) method.[39] The cut-off

energy for the planewave basis set is 500 eV, giving good convergence of the energies and structures. The criteria for terminating self-consistent field and the geometry optimization were set to 10^{-6} eV and 10^{-3} eV/Å, respectively. The Brillouin zone integration was performed using the Γ-centered symmetry reduced Monkhorst−Pack meshes with a fine resolution of $2\pi\times1/40$ $Å^{-1}$.

The equation of state (EOS) for the crystalline structures B_4C, $B_{13}C_2$, and $B_{12}Si_2$ were obtained by compressing or stretching the equilibrium supercell with a strain of 0.02 along each direction. At each strain, the structure was optimized with fixed cell parameters. The ideal shear deformation was applied to obtain the energies and structures at finite shear strain for crystalline phases $B_{12}Si_2$, $B_{13}C_2$-GBI, $B_{13}C_2$-GBII, Si-doped $B_{13}C_2$-GBI, and Si-doped $B_{13}C_2$-GBII. The shear strain was employed along a particular slip system while relaxing the structure to minimize the other five stress components.[40] For $B_{12}Si_2$, a $2 \times 2 \times 2$ supercell with 112 atoms was used for shear deformation along the slip system of $(100)_r[001]_r$. The shear deformation of all GB structures was applied parallel to GB planes using a supercell with ~200 atoms. This force field was developed based on previous ReaxFF for B_4C.[11]

3. RESULTS AND DISCUSSION

3.1 Development of ReaxFF for B-C-Si

The parameterization of the ReaxFF force field for B-C-Si was firstly improved based on quantum mechanics (QM) simulations on crystalline phases ($B_{13}C_2$, B_4C, and $B_{12}Si_2$) and microstructures (GBs, and Si-doped GBs). Our QM simulations indicated that Si prefers to be incorporated into $B_{13}C_2$ rather than B_4C. Therefore, to improve the ReaxFF for B_4C, QM data on $B_{13}C_2$ microstructures was added to the training set for developing the B-C-Si force field. The training set for developing ReaxFF includes QM results for

i. the equation of state (EOS) of $(B_{11}C_p)$(CBC) (hereafter B_4C) and (B_{12})(CBC) (hereafter $B_{13}C_2$)
ii. shear deformation of B_4C and $B_{13}C_2$ of two specific GB structures for $B_{13}C_2$ and B_4C (designed as GBI and GBII),
iii. the heat of formation of B_4C and $B_{13}C_2$,

iv. the energy difference between GBs and crystalline structures (B_4C and $B_{13}C_2$),
v. shear deformation of $B_{12}Si_2$ and Si-doped GB structures (GBI and GBII),
vi. heat of formation of $B_{12}Si_2$, and
vii. heat of formation of two Si-doped GB structures.

The EOS and shear deformation results for B-C systems from both ReaxFF and QM are compared in Fig. 1(A-F) while the calculated values for heat of formation and energy differences are listed in Table S1 and S2 of the Supplementary Material (SM). The shear deformations of $B_{12}Si_2$, Si-doped GBI, and Si-doped GBII are shown in Fig. 1(G-I) and the heat of formation for $B_{12}Si_2$ and Si-doped GB structures are listed in Table S1. Overall, the predictions from ReaxFF are consistent with QM results, validating the new ReaxFF for B-C-Si system. Inserting Si into $B_{13}C_2$-GBI and $B_{13}C_2$-GBII leads to negative heats of formation from QM simulations, suggesting that Si prefers both GB models of $B_{13}C_2$. The force field parameters are listed in the SM.

3.2 Shear deformation and failure mechanism of B_4C and $B_{13}C_2$

The new B-C-Si ReaxFF was used in MD simulations to examine the shear deformation and failure mechanism of $B_{13}C_2$ which were compared to the ground state B_4C. Here, B_4C is sheared along the most plausible slip system of $(001)_r[100]_r$.[10, 11] The simulation model was constructed with cell lengths a=2.08nm, b=2.08nm, and c=8.02nm for B_4C and a=2.11nm, b=2.11nm, and c=7.26nm for $B_{13}C_2$, leading to supercells with ~4000 atoms. These models of B_4C and $B_{13}C_2$ are shown in Fig. 2(A) and (B), respectively.

The shear-stress-shear-strain relationships of B_4C and $B_{13}C_2$ are shown in Fig. 2(C). The predicted critical shear stress of B_4C is 46.7 GPa, which is comparable with the value (45 GPa) from our previous ReaxFF simulations.[11] This value is higher than the ideal shear strength (37.2 GPa) from QM simulations[10] possibly due to the fixed volume shear deformation. The failure process of B_4C during shear deformation is shown in Fig. 3. Fig. 3(A) displays the intact structure before shear. As the shear strain increases to 0.325, the shear stress increases to its maximum value of 46.7 GPa, with all icosahedra are deformed elastically under shear stress, as shown in Fig. 3(B). Then, at 0.529 shear strain, the amorphous band forms, which dramatically releases shear stress to 22.2 GPa, as shown in Fig. 3(C). Finally, as the shear strain increases to 1.303, a cavity forms within the amorphous band to

further relax the shear stress, as shown in Fig. 3(D). This failure process and amorphous band formation are similar to our previous ReaxFF study.[11]

Comparing to B_4C, $B_{13}C_2$ shows a much lower critical shear stress of 28.6 GPa, suggesting that it is intrinsically weaker than B_4C, as shown in Fig. 2. However, a kink is observed in the shear-stress-shear-strain relationship, suggesting a two-step failure process under shear deformation, which is different from B_4C. The failure process of $B_{13}C_2$ is shown in Fig. 4. Fig. 4(A) shows the intact structure before shear. As the shear strain increases to 0.254, the structure deforms elastically without structural failure. However, at 0.341 shear strain, the B-B bonds connecting two nearby layers of icosahedra have broken. Meanwhile, some icosahedra rotate to relax the shear stress from 25.5 GPa to 20.0 GPa, as shown in Fig. 4(B). Then, with increased shear strain, more icosahedra start to rotate. At 0.510 strain, the region of rotated icosahedra expands to the whole structure, as shown in Fig. 4(C). Meanwhile, the shear stress increases to the maximum value of 28.6 GPa. Then the amorphous band forms as the shear strain increases further to 0.848 (Fig. 4(D)). Finally, at 1.480 shear strain, a cavity forms within the amorphous band, as shown in Fig. 4(E). The critical shear strain (0.848) for amorphization in $B_{13}C_2$ is much larger than that of B_4C (0.529), suggesting that **$B_{13}C_2$ has a larger strain to failure than B_4C.** The improvement of ductility is because the icosahedra in $B_{13}C_2$ favor rotation rather than breaking the icosahedra bonds to relax stress during shear. This postpones the deconstruction of icosahedra. However, this rotation of icosahedra also decreases the strength of $B_{13}C_2$. The results also indicate that boron enrichment can help mitigate the amorphization in boron carbide, which agrees with the findings in previous experiment.[17–19] To obtain the intrinsic error of our simulations, a 2nd simulation was performed by reassigning the velocity distribution at 300 K before equilibrium. Following the same procedure as the first simulation, the shear-stress-shear-strain relationship is computed and shown in Fig. S2(A). The obtained critical stress for the 2nd simulation is 29.0 GPa, which is ~1.4% different than the first simulation, suggesting that the intrinsic error is about 1.4%. Also, the failure mechanism is the same for both simulations.

3.3 The effect of doping Si in the GB region on shear deformation of $B_{13}C_2$-GBI.

Next, the new ReaxFF was applied to examine shear deformation of polycrystalline boron carbide containing GBs. The QM simulations indicated that Si prefers to be doped into the $B_{13}C_2$ rather than B_4C. Particularly, the heat of formation of Si-doped $B_{13}C_2$-GBI and $B_{13}C_2$-GBII is -0.647 eV and -1.135eV, which is more negative than that of Si-doped B_4C-GBs (1.785 eV for GBI and -0.079eV for GBII). Therefore, we focus on RMD simulations of the Si-doped $B_{13}C_2$ systems. For the GB structures of $B_{13}C_2$, the $B_{13}C_2$-GBI model was firstly selected with two grains orientated along $[111]_r$ and $[\bar{1}\bar{1}3]_r$ along the "c" direction. In this GBI model, the icosahedral clusters are not deconstructed. The DFT study of the deformation of this GB for B_4C was published previously.[28] In contrast to the previous GB model, the number of crystalline layers was increased between the two GB regions to construct a supercell with cell lengths of a=4.27nm, b=4.27nm, and c=8.21nm, leading to 18,240 atoms, as shown in Fig. 5(A). In this model, the shear direction ("a" axis) is parallel to the GB regions. In order to determine the most plausible slip direction (parallel or perpendicular to GBs) for GBI structures, a model with the "a" axis perpendicular to the GB regions was constructed, corresponding to the $[\bar{1}\bar{1}3]_r$ direction for Grain A and the $[111]_r$ direction for Grain B, as shown in Fig. S5(A). This leads to the cell lengths of a=5.61nm, b=2.13nm, and c= 7.58nm.

The shear-stress-shear-strain relationships of GBI structures along shear directions parallel or perpendicular to the GBs are shown in Fig. S3. For the shear deformation parallel to the GBs, we sheared the model along both negative and positive directions and compared the critical stress. The results show that the negative direction, which corresponds to the $[\bar{1}00]_r$ direction for Grain A and $[\bar{1}10]_r$ for Grain B, has a lower critical shear stress of 25.4 GPa compared to 33.5GPa for the positive direction parallel to GBs and 37.8GPa for the direction perpendicular to GBs, suggesting that it is more plausible for $B_{13}C_2$-GBI. This value is lower than that of single-crystal $B_{13}C_2$ (28.6 GPa), suggesting that the presence of GB weakens the $B_{13}C_2$ with the amorphization initiating from the GB regions in polycrystalline $B_{13}C_2$, as shown in Fig. S4. Moreover, a kink is observed in the stress-strain relationship (Fig. S3), suggesting that the failure process can be partitioned into two steps, as shown in Fig. 5. The intact structure before shear is shown in Fig. 5(A). As the shear strain increases to 0.296, the icosahedral clusters near the GB region are deconstructed, as shown in Fig. 5(B). This also releases the shear stress from the maximum value of 25.4 GPa to 21.2 GPa. Meanwhile, the icosahedra in the crystalline region of Grain B are deformed without deconstruction. Then, as the

shear strain increases to 0.635, the shear stress gradually increases to 23.5 GPa and releases the stress to 21.3 GPa. This is because the icosahedral clusters in the crystalline layer are deconstructed, initiating the amorphization in this GB structure, as shown in Fig. 5(C). Finally, an amorphous band forms in the region of Grain B at 1.062 shear strain to release the shear stress to ~19 GPa, as shown in Fig. 5(D). After that, the 2nd simulation on shear deformation along the negative direction was also performed, similar to crystal $B_{13}C_2$, to examine the intrinsic error of the RMD simulations. The obtained shear-stress-shear-strain relationship is shown in Fig. S2(B) and the intrinsic error for RMD is also ~1.5% which is similar to crystalline $B_{13}C_2$.

The failure mechanism along the positive direction parallel to the GBs is similar to the failure process along negative direction parallel to the GBs, as shown in Fig. S5. The intact structure is shown in Fig. S5(A). The first step of structural failure arises from the deconstruction of icosahedral clusters in the GB region at 0.392 shear strain, as shown in Fig. S5(B). This releases the shear stress from the maximum value of 29.8 GPa to 26.0 GPa. Then, at 0.920 shear strain, the icosahedral clusters in the crystalline layers are deconstructed to form an amorphous band, leading to the further release of shear stress to 15.5 GPa, as shown in Fig. S5(C). This corresponds to the second step of structural failure.

The failure mechanism for shear perpendicular to the GBs is shown in Fig. S6. The structural failure also arises from the deconstruction of icosahedral clusters in the GB region, as shown in Fig. S6(B). All these results regarding the failure mechanism of the $B_{13}C_2$-GBI structure indicate that the GB region is weaker than the crystalline region. Hence, the failure of the $B_{13}C_2$-GBI model occurs when the icosahedra in the GB region deconstruct.

Then, 32 Si atoms were added into the GB region (doping concentration: ~0.09 at%) to construct the Si-doped GB model. Shear deformation was applied to examine the effects of Si doping. Here, the Si-doped GBI structure was sheared along the negative direction parallel to the GB since it is the most plausible slip direction for GBI. The shear-stress-shear-strain relationship for Si-doped GBI is shown in Fig. 6 and compared to GBI without Si. Doping with Si increased the critical shear stress to 30.2 GPa, which is 4.8 GPa higher than that of pure GBI (25.4 GPa). This is comparable to the crystalline

$B_{13}C_2$ (28.6 GPa), suggesting that **doping Si atoms in the GB region can dramatically strengthen the GBI structures by increasing the stress threshold for amorphization.**

The failure mechanism of the Si-doped $B_{13}C_2$-GBI structure is displayed in Fig. 7. The initial structure before is shown in Fig. 7(A). As the shear strain increases to 0.326, the icosahedra in the GB region are deconstructed, as shown in Fig. 7(B), releasing the shear stress from 25.1 GPa to 21.1 GPa. Then, with the increase of shear strain, the icosahedra near the GB region in Grain A of Si-doped GBI are rotated as shear strain increase to 0.612, which is similar to the first step of the failure process for crystalline $B_{13}C_2$. This is different from the failure mechanism of pure GBI that the icosahedra in the region of Grain B are deformed and then deconstructed to form an amorphous shear band. Meanwhile, the icosahedra in the Grain B region are deformed. However, none of them is deconstructed at this shear strain, as shown in Fig. 7(C). With further increase of shear strain, the rotated icosahedral layers are gradually expanded to the whole crystalline region of Grain A. At 0.776 shear strain, 5-layers icosahedra are rotated, as shown in Fig. 7(D). Finally, at 1.075 shear strain, the rotated icosahedra in Grain A are deconstructed to form an amorphous band, as shown in Fig. 7(E).

The $B_{13}C_2$-GBI has a lower critical shear stress of 25.4 GPa under ideal shear deformation, compared to 28.6 GPa for crystalline $B_{13}C_2$, suggesting that the presence of GBs in the polycrystal lowers the strength of $B_{13}C_2$ while favoring the formation of the amorphous band.

However, doping Si atoms into the GB region increases the stress threshold for amorphization as well as the strength of the GBI structure. This is due to the change in failure mechanisms between pure GBI and Si-doped GBI. For pure GBI, the icosahedra in Grain B deform and then deconstruct to form the amorphous shear band. However, for Si-doped GBI, the icosahedra in Grain A rotate first and later deconstruct to form the amorphous band.

3.4 The effect of doping Si in the GB region on shear deformation of $B_{13}C_2$-GBII.

In addition to GBI, the shear deformation of $B_{13}C_2$-GBII was examined and explored how Si doping affects the deformation process. The GBII model has broken cages along the GBs, in contrast to the GBI model. Firstly, the GBII model was constructed with Grain A along $[2\bar{1}\bar{1}]$ and Grain B along $[\bar{2}11]$ along "c" direction. The orientations are similar to the GBII model of B_4C in our previous

DFT study.[28] Then, a supercell was created by increasing the crystalline layers between two GBs by 4 layers compared to our previous DFT.[28] The constructed supercell has cell lengths of a=4.93nm, b=2.21nm, and c=6.01nm, leading to 8,720 atoms, as shown in Fig. 9(A). For the shear deformation, the orientations for Grain A and Grain B are the same. For the GBII model, it is only sheared parallel to GBs.

The shear-stress-shear-strain relationship for the pure GBII is shown in Fig. 8. The critical shear stress is 28.0 GPa, which is slightly lower than crystalline $B_{13}C_2$ (28.6 GPa), as shown in Fig. S4. In order to demonstrate that this small decrease in critical stress of GBII is not caused by intrinsic error of the RMD simulation, the standard deviation for the shear stress fluctuation was computed to be 0.166GPa. This suggests that the critical stress of GBII is lower than the value of crystalline $B_{13}C_2$**.** The failure process of the GBII structure is shown in Fig. 9. The intact structure is shown in Fig. 9(A). Fig. 9(B) exhibits the structural failure in the GB region at 0.297 shear strain. This slightly releases shear stress from 27.1 GPa to 26.2 GPa. Meanwhile, the icosahedra in part of the crystalline region of Grain B also deform under shear stress. However, they do not deconstruct. At 0.503 shear strain, all icosahedra in Grain B are deformed, as shown in Fig. 9(C). Also, some icosahedra at the bottom of the cell start to deconstruct, which initiates amorphization. Then, as shear strain increases to 0.723, the amorphous band in that crystalline region forms, as shown in Fig. 9(D).

Then, 8 Si atoms were added into the GB region, leading to a doping concentration of ~0.09 at%, as shown in Fig. 10(A). This doping concentration is same with Si-doped GBI. This Si-doped GBII was sheared along the same direction as the pure GBII. The shear-stress-shear-strain relationship is shown in Fig. 8. The critical shear stress of Si-doped GBII is 30.5 GPa, which is higher than GBII (28.0 GPa). Thus, Si doping can help strengthen the GBII. The failure mechanism of the Si-doped GBII is similar to the failure process of the pure GBII structure, as shown in Fig. 10. The intact structure is shown in Fig. 10(A). Then, at 0.349 shear strain, the structure in the GB region fails while the icosahedra in the crystalline region of Grain B start to deform, as shown in Fig. 10(B). This slightly releases the shear stress from the maximum value of 28.5 GPa to 26.0 GPa. Note that this critical shear stress is slightly higher than that of pure GBII (27.1 GPa), suggesting that Si doping can increase the stress threshold for the deconstruction of icosahedra in the GB region. Then, at 0.614 shear strain, the icosahedra in the bottom layers of Grain B start to deconstruct, initiating

amorphization and relaxation of the shear stress, as shown in Fig. 10(C). Finally, at 0.818 shear strain, the icosahedra in that region completely deconstruct and the amorphous band forms, as shown in Fig. 10(D). The combination of stress-strain relationship and failure process suggests that doping Si into the GB region of GBII can increase the stress threshold for both structural failures in the GB region and for amorphous shear band formation.

The critical shear stress of 28.0 GPa for $B_{13}C_2$-GBII is lower than the 28.6GPa of crystalline $B_{13}C_2$, suggesting that amorphization prefers to initiate near the GBII region of polycrystalline boron carbide. However, adding Si into the GB region increases the strength of GBII and helps mitigate the formation of amorphous shear band in GBII, similar to the Si doping in GBI.

4. CONCLUSION

In summary, ReaxFF RMD simulations were applied to examine how Si doping in GBs affects the shear deformation and failure mechanism of boron carbide. Firstly, the shear deformation of $B_{13}C_2$ was examined and compared to B_4C. Then, the shear deformation of two specific GB models of $B_{13}C_2$ including $B_{13}C_2$-GBI and $B_{13}C_2$-GBII were examined. After that, Si atoms were added into their GB regions to illustrate the effect of Si doping on the mechanical properties of GB structures. The main findings are:

1. $B_{13}C_2$ has a lower critical shear strength (28.6GPa) compared to B_4C (46.7GPa), but $B_{13}C_2$ exhibits a larger critical strain for amorphization, 0.848 compared to 0.529, suggesting that boron enrichment helps mitigate amorphization in boron carbide.

2. The critical shear stresses for $B_{13}C_2$-GBI and $B_{13}C_2$-GBII models, 25.4GPa and 28.0GPa, are lower than that of crystalline $B_{13}C_2$, 28.6GPa, suggesting that the GB models are weaker than the crystal phase and that the amorphous band prefers to initiate near GB regions.

3. For both $B_{13}C_2$-GBI and $B_{13}C_2$-GBII, adding Si atoms into GB regions increases their shear strength and stress threshold for amorphous band formation: 30.2GPa and 30.5GPa compared to

25.4GPa and 28.0GPa This suggests that doping Si in GBs helps mitigate amorphization in boron carbide.

The present study focuses on two special GB models. In future studies, it is important to examine the effects of Si dopants on more general GB structures, such as tilt and twist boundaries. Our results provide an atomic-level explanation consistent with experimental findings that doping Si into boron carbide helps mitigate amorphization.[33] Our findings provide a basis for future materials design to improve ductility of super-hard boron carbide.

Acknowledgements

Y.D. and Q. A. were supported by National Science Foundation with funding number CMMI-1727428. M.Y. and W.A.G. were supported by the Materials in Extreme Dynamic Environments (MEDE) program (ARL W911NF-12-2-0022).

References

1. Caruso AN, Dowben PA, Balkir S, *et al.* The all boron carbide diode neutron detector: Comparison with theory. *Mater Sci Eng B*. 2006;135(2):129–133.
2. Deng J. Erosion wear of boron carbide ceramic nozzles by abrasive air-jets. *Mater Sci Eng A*. 2005;408:227–233.
3. An Q, Goddard WA. Boron suboxide and boron subphosphide crystals: Hard ceramics that shear without brittle failure. *Chem Mater*. 2015;27(8):2855–2860.
4. Domnich V, Reynaud S, Haber RA, Chhowalla M. Boron carbide: Structure, properties, and stability under stress. *J Am Ceram Soc*. 2011;94(11):3605–3628.
5. Chen M, McCauley JW, Hemker KJ. Shock-induced localized amorphization in boron carbide. *Science*. 2003;299(5612):1563–1566.
6. Reddy KM, Liu P, Hirata A, Fujita T, Chen MW. Atomic structure of amorphous shear bands in boron carbide. *Nat Commun*. 2013;4:2483.

7. Zhao S, Kad B, Remington BA, *et al.* Directional amorphization of boron carbide subjected to laser shock compression. *Proc Natl Acad Sci U S A*. 2016;113(43):12088–12093.

8. Gosset D, Miro S, Doriot S, Victor G, Motte V. Evidence of amorphisation of B4C boron carbide under slow, heavy ion irradiation. *Nucl Instruments Methods Phys Res Sect B Beam Interact with Mater Atoms*. 2015;365:300–304.

9. Chen M, McCauley JW. Mechanical scratching induced phase transitions and reactions of boron carbide. *J Appl Phys*. 2006;100(12):123517.

10. An Q, Goddard W, Cheng T. Atomistic explanation of shear-induced amorphous band formation in boron carbide. *Phys Rev Lett*. 2014;113(9):095501.

11. An Q, Goddard WA. Atomistic Origin of Brittle Failure of Boron Carbide from Large-Scale Reactive Dynamics Simulations: Suggestions toward Improved Ductility. *Phys Rev Lett*. 2015;115(10):105501.

12. Tang B, He Y, Goddard WA, An Q. First principles predicting enhanced ductility of boride carbide through magnesium microalloying. *J Am Ceram Soc*. 2019;102(9):5514–5523.

13. Nikzad L, Orrù R, Licheri R, Cao G. Fabrication and formation mechanism of B 4 C - TiB 2 composite by reactive spark plasma sintering using unmilled and mechanically activated reactants. *J Am Ceram Soc*. 2012;95(11):3463–3471.

14. He Y, Shen Y, Tang B, An Q. Strengthening boron carbide through lithium dopant. *J Am Ceram Soc*. 2020;103(3):2012–2023.

15. Hillebrecht H, Vojteer N, Sagawe V, Hofmann K, Albert B. Synthesis and Characterization of Li-containing Boron Carbide r-Li ~1 B 13 C 2. *Zeitschrift fur Anorg und Allg Chemie*. 2019;645(3):362–369.

16. Adasch V, Schroeder M, Kotzott D, Ludwig T, Vojteer N, Hillebrecht H. Synthesis , Crystal Structure , and Properties of Mg x B $_{50}$ C $_{8}$ or Mg $_{x}$ (B $_{12}$) $_{4}$ (CBC) $_{2}$ (C $_{2}$) $_{2}$ (x) $_{2.4-4}$). *J Am Ceram Soc*. 2010;132(39):13723–13732.

17. Chauhan A, Schaefer MC, Haber RA, Hemker KJ. Experimental observations of amorphization

in stoichiometric and boron-rich boron carbide. *Acta Mater*. 2019;181:207–215.

18. Schaefer MC, Haber RA. Amorphization Mitigation in Boron-Rich Boron Carbides Quantified by Raman Spectroscopy. *Ceramics*. 2020;3(3):297–305.
19. Chauhan A, Schaefer MC, Haber RA, Hemker KJ. Observed Mitigation of Local Amorphization in Boron-Rich Boron Carbide. *SSRN Electron J*. 2019;in press.
20. Yan X, Zhou X, Wang H. E ff ect of Additive Ti 3 SiC 2 Content on the Mechanical Properties of B 4 C – TiB 2 Composites Ceramics Sintered. *Materials (Basel)*. 2020;13:4616.
21. Kim H, Koh Y-H, Kim H-E. Densification and Mechanical Properties of B4C with Al2O3 as a Sintering Aid. *J Am Ceram Soc*. 2000;83(11):2863–2865.
22. Xie KY, Kuwelkar K, Haber RA, LaSalvia JC, Hemker KJ, Hay R. Microstructural Characterization of a Commercial Hot-Pressed Boron Carbide Armor Plate. *J Am Ceram Soc*. 2016;99(8):2834–2841.
23. An Q, Goddard WA. Ductility in Crystalline Boron Subphosphide (B12P2) for Large Strain Indentation. *J Phys Chem C*. 2017;121(30):16644–16649.
24. An Q, Goddard WA. Microalloying boron carbide with silicon to achieve dramatically improved ductility. *J Phys Chem Lett*. 2014;5(23):4169–4174.
25. Zhang Z, Du X, Li Z, Wang W, Zhang J, Fu Z. Microstructures and mechanical properties of B4C-SiC intergranular/intragranular nanocomposite ceramics fabricated from B4C, Si, and graphite powders. *J Eur Ceram Soc*. 2014;34(10):2153–2161.
26. Yamada S, Hirao K, Yamauchi Y, Kanzaki S. High strength B4C- TiB2 composites fabricated by reaction hot-pressing. *J Eur Ceram Soc*. 2003;23(7):1123–1130.
27. Chen MW, McCauley JW, LaSalvia JC, Hemker KJ. Microstructural characterization of commercial hot-pressed boron carbide ceramics. *J Am Ceram Soc*. 2005;88(7):1935–1942.
28. Yang X, Coleman SP, Lasalvia JC, Goddard WA, An Q. Shear-Induced Brittle Failure along Grain Boundaries in Boron Carbide. *ACS Appl Mater Interfaces*. 2018;10(5):5072–5080.

29. Guo D, Song S, Luo R, *et al.* Grain Boundary Sliding and Amorphization are Responsible for the Reverse Hall-Petch Relation in Superhard Nanocrystalline Boron Carbide. *Phys Rev Lett*. 2018;121(14):145504.

30. Shen Y, Fuller J, An Q. Mitigating the formation of amorphous shear band in boron carbide. *J Appl Phys*. 2021;129(14):140902.

31. Behler KD, Marvel CJ, LaSalvia JC, Walck SD, Harmer MP. Observations of grain boundary chemistry variations in a boron carbide processed with oxide additives. *Scr Mater*. 2018;142:106–110.

32. Mashhadi M, Taheri-Nassaj E, Sglavo VM, Sarpoolaky H, Ehsani N. Effect of Al addition on pressureless sintering of B4C. *Ceram Int*. 2009;35(2):831–837.

33. Xiang S, Ma L, Yang B, *et al.* Tuning the deformation mechanisms of boron carbide via silicon doping. *Sci Adv*. 2019;5:0352.

34. Plimpton S. Fast parallel algorithms for short-range molecular dynamics. *J Comput Phys*. 1995;117(1):1–19.

35. See Supplemental Material at xxx for (i) reaxFF parameters, (ii) Table S1 and S2, and (iii) Fig S1 to S4.

36. Kresse G, Furthmuller J. Efficiency of ab-initio total energy calculations for metals and semiconductors using a plane-wave basis set. *Comput Mater Sci*. 1996;6(1):15–50.

37. Kresse G, Furthmuller J. Efficient iterative schemes for ab initio total-energy calculations using a plane-wave basis set. *Phys Rev B*. 1996;54(16):11169.

38. Kresse G, Hafner J. Abinitio molecular-dynamics for liquid-metals. *Phys Rev B*. 1993;47(1):558–561.

39. Kresse G, Joubert D. From ultrasoft pseudopotentials to the projector augmented-wave method. *Phys Rev B*. 1999;59(3):1758–1775.

40. Roundy D, Krenn CR, Cohen ML, Morris, Jr JW. Ideal shear strengths of fcc aluminum and

copper. *Phys Rev Lett*. 1999;82(13):2713–2716.

Figure Captions

FIGURE 1 Comparison between ReaxFF and QM results for equation of state of (A) B_4C and (B) $B_{13}C_2$, and shear deformation of: (C) B_4C, (D) $B_{13}C_2$, (E) $B_{13}C_2$-GBI, (F) $B_{13}C_2$-GBII; (G) $B_{12}Si_2$; (H) Si-doped $B_{13}C_2$-GBI, and (I) Si-doped $B_{13}C_2$-GBII.

FIGURE 2 (A) and (B) The models for shear of B_4C and $B_{13}C_2$, respectively; (C) the shear-stress-shear-strain relationships of crystalline B_4C and $B_{13}C_2$ along the $(001)_r[100]_r$ slip system. The blue and yellow balls represent the boron and carbon atoms, respectively.

FIGURE 3 Failure mechanism of crystalline B_4C along the $(001)_r[100]_r$ slip system. (A) The intact structure; (B) the structure at 0.325 shear strain; (C) the formation of amorphous shear band at 0.529 shear strain; (D) cavitation within the amorphous band at 1.303 strain. The blue and yellow balls represent the boron and carbon atoms, respectively.

FIGURE 4. Deformation and failure mechanism of crystalline $B_{13}C_2$ for shear along the $(001)_r[100]_r$ slip system. (A) The intact structure; (B) the structure at 0.341 shear strain *before* rotation of icosahedra; (C) the rotation of icosahedra at 0.510 shear strain (D) the formation of amorphous band at 0.848 strain; (D) cavitation within the amorphous band at 1.480 strain. The blue and yellow balls represent the boron and carbon atoms, respectively.

FIGURE 5. Deformation and mechanism of $B_{13}C_2$-GBI for shear parallel to GB. (A) The intact structure; (B) the deconstruction of icosahedra near GB region at 0.296 shear strain; (C) the initiation of amorphization at 0.635 shear strain; (D) the formation of amorphous band at 1.062 shear strain. The blue and yellow balls represent the boron and carbon atoms, respectively.

FIGURE 6 Shear-stress-shear-strain relationships of $B_{13}C_2$ GBI-model with/without doped Si.

FIGURE 7 Deformation and mechanism of Si-doped $B_{13}C_2$-GBI for shear along the negative direction parallel to the GB. (A) The intact structure; (B) the deconstruction of icosahedra near GB region at 0.326 shear strain; (C) the rotation of one-layer of icosahedra in Grain A at 0.612 shear strain; (D) the rotation of 5 icosahedral layers in Grain A at 0.776 shear strain; (E) the formation of the amorphous band in Grain A at 1.075 shear strain. The blue, yellow, and red balls represent the boron, carbon, and silicon atoms, respectively. The black dashed line indicates the GBs.

FIGURE 8 Shear-stress-shear-strain relationships of $B_{13}C_2$ GBII-model with/without doped Si.

FIGURE 9. Deformation and failure mechanism of $B_{13}C_2$-GBII shear parallel to GB. (A) The intact structure; (B) structural failure in GB region at 0.297 shear strain; (C) the deformation of icosahedra in Grain B at 0.503 shear strain; (D) the formation of amorphous band in Grain B at 0.723 shear strain. The blue and yellow balls represent the boron and carbon atoms, respectively. The black dashed line represents GBs.

FIGURE 10. Deformation and failure mechanism of $B_{13}C_2$-GBII model with doped Si shear parallel to GB. (A) The intact structure; (B) structural failure in GB region at 0.349 shear strain; (C) the deconstruction of icosahedra in bottom layers of Grain B at 0.614 shear strain; (D) the formation of amorphous band in Grain B at 0.818 shear strain. The blue, yellow, and red balls represent the boron, carbon, and silicon atoms, respectively.

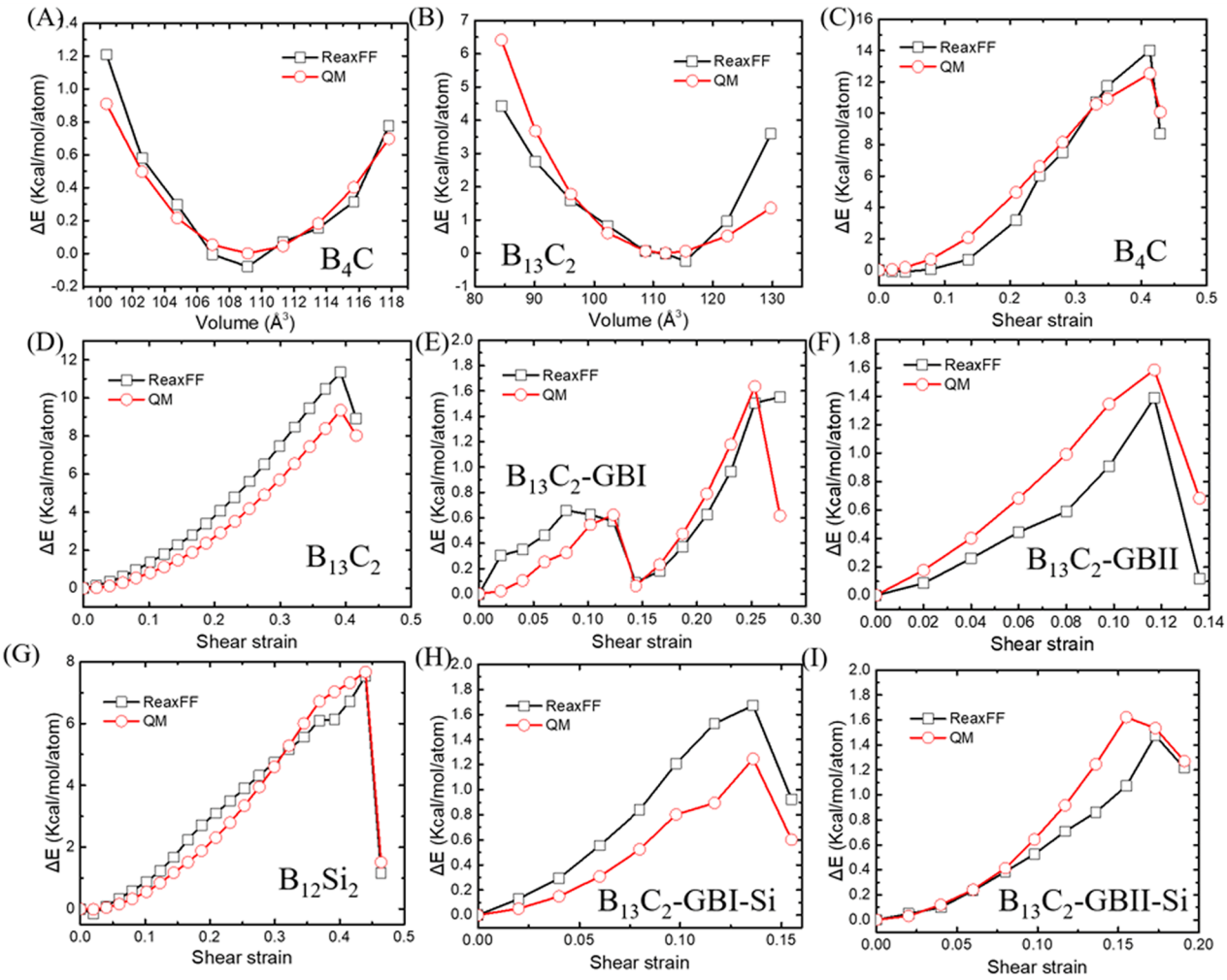

jace_18028_f1.tif

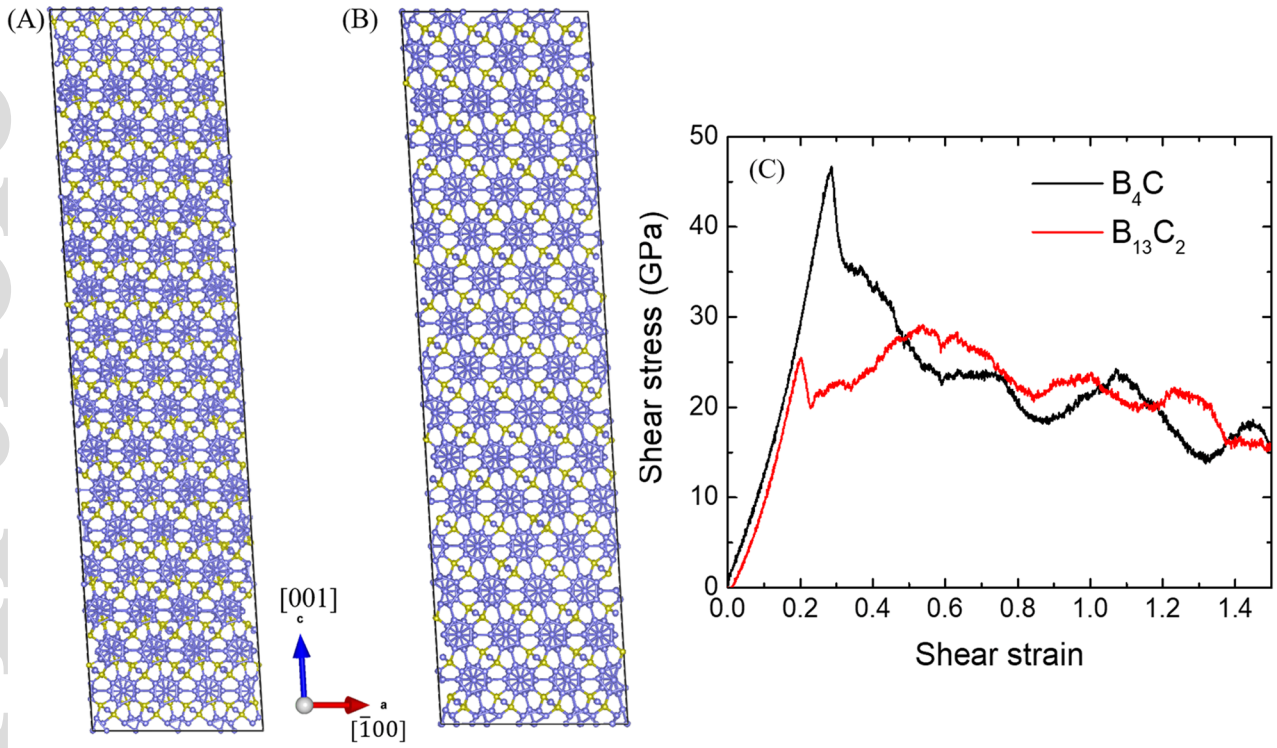

jace_18028_f2.tif

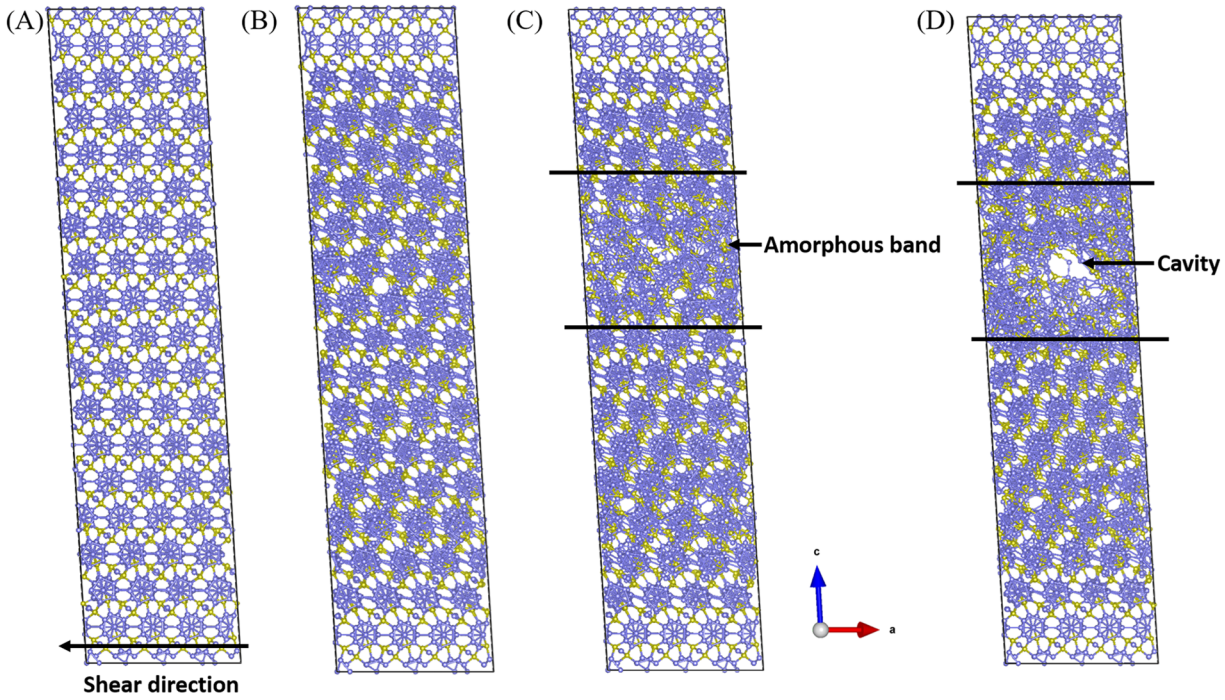

jace_18028_f3.tif

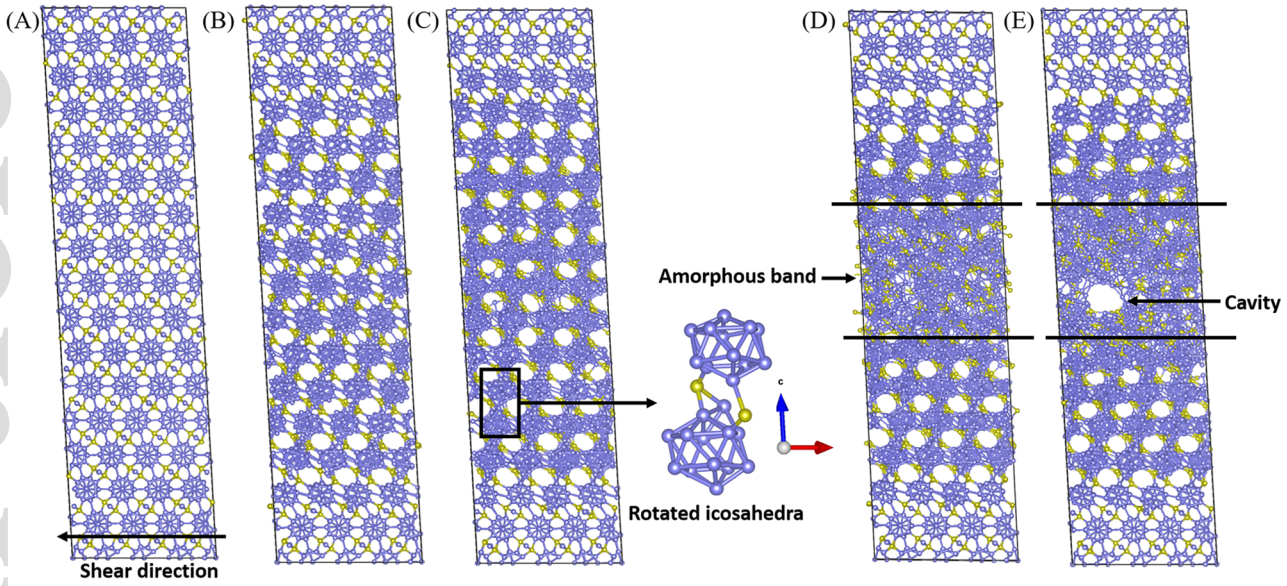

jace_18028_f4.tif

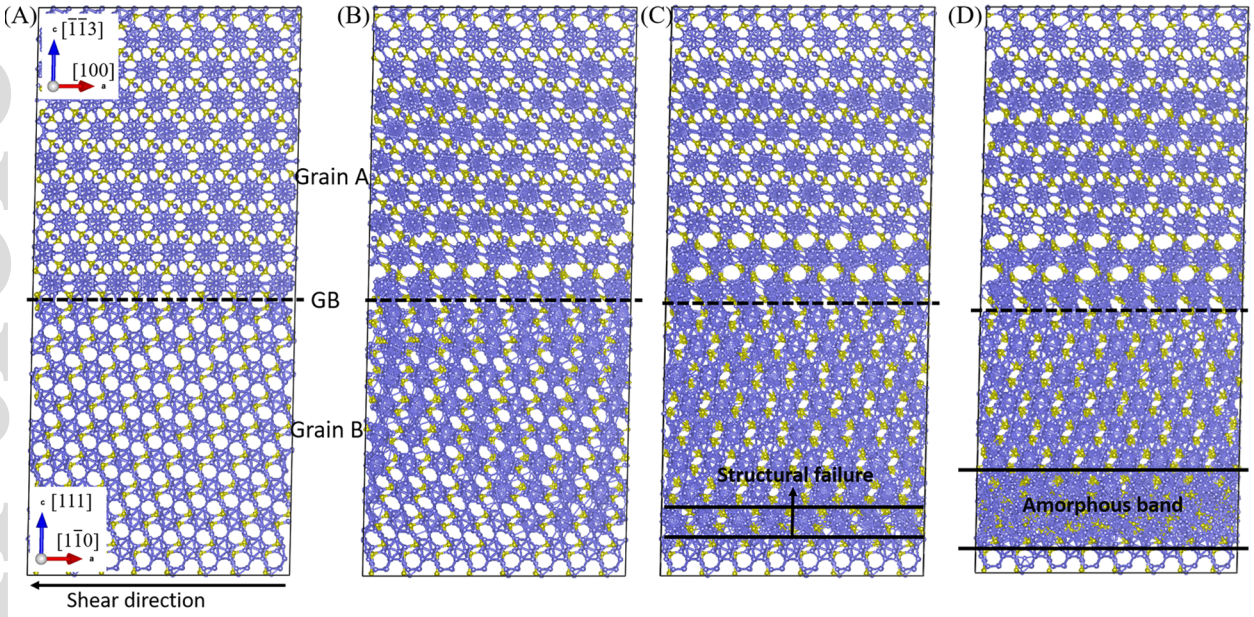

jace_18028_f5.tif

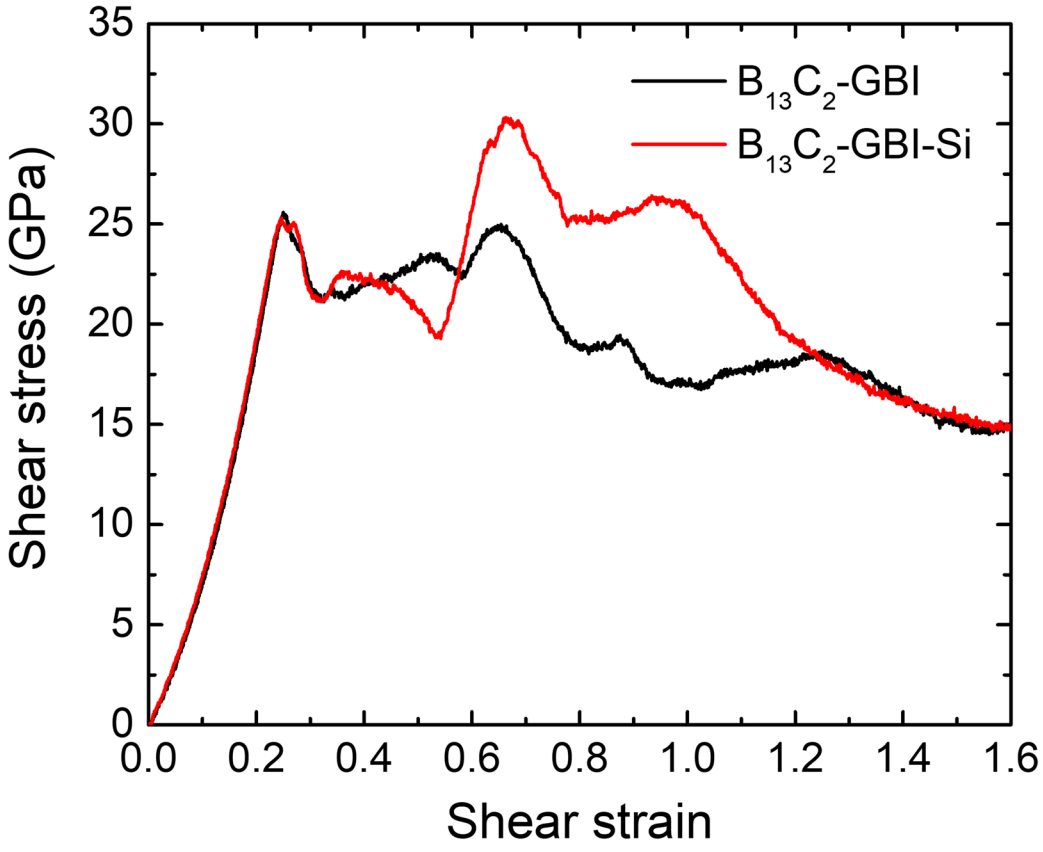

jace_18028_f6.tif

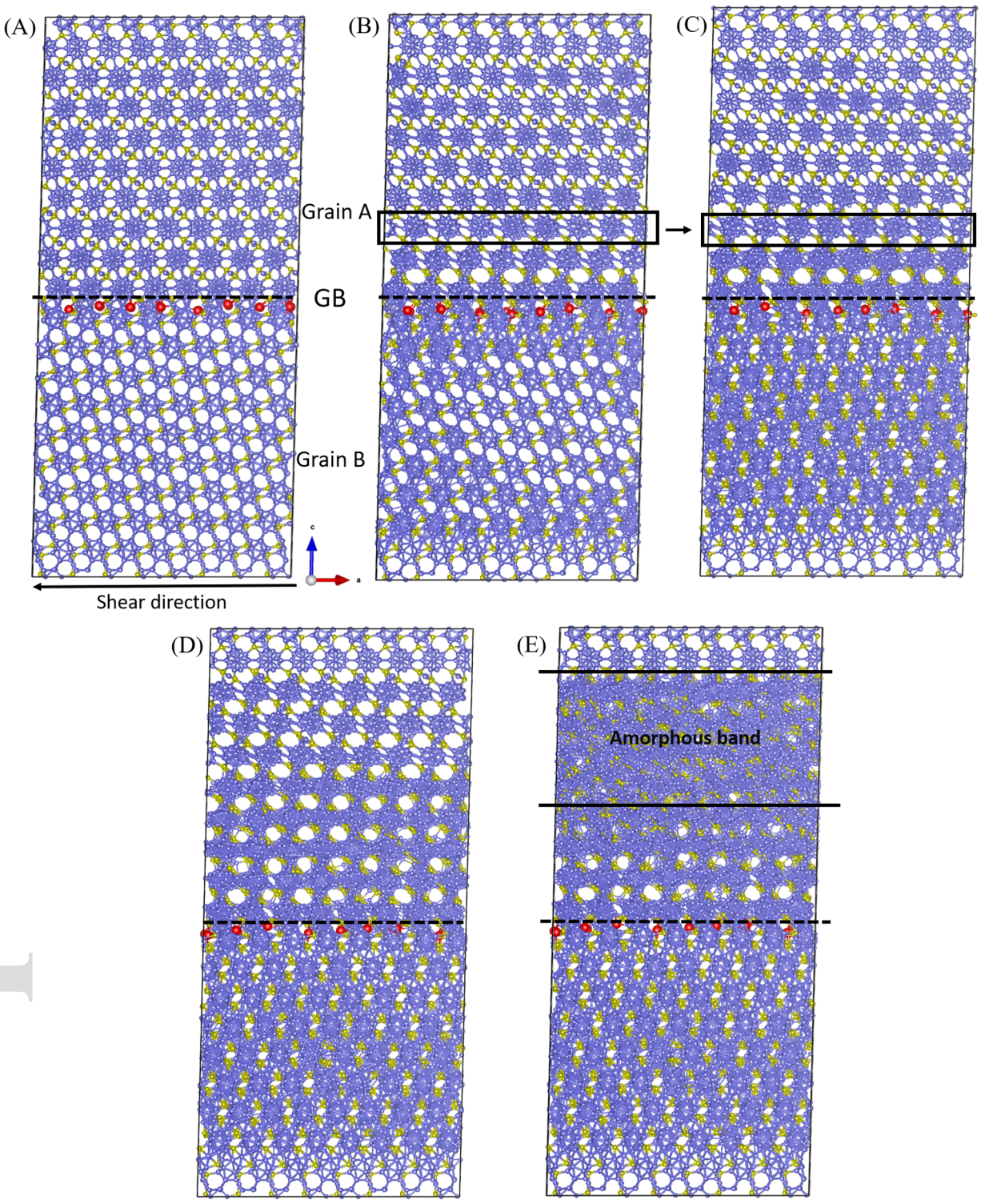

jace_18028_f7.tif

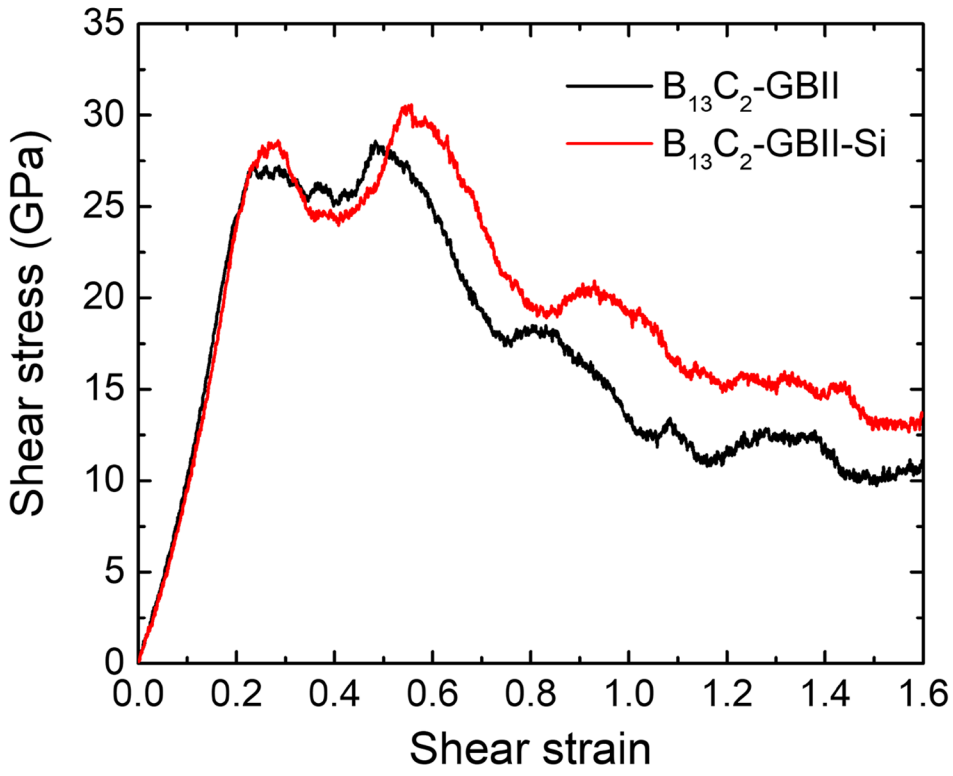

jace_18028_f8.tif

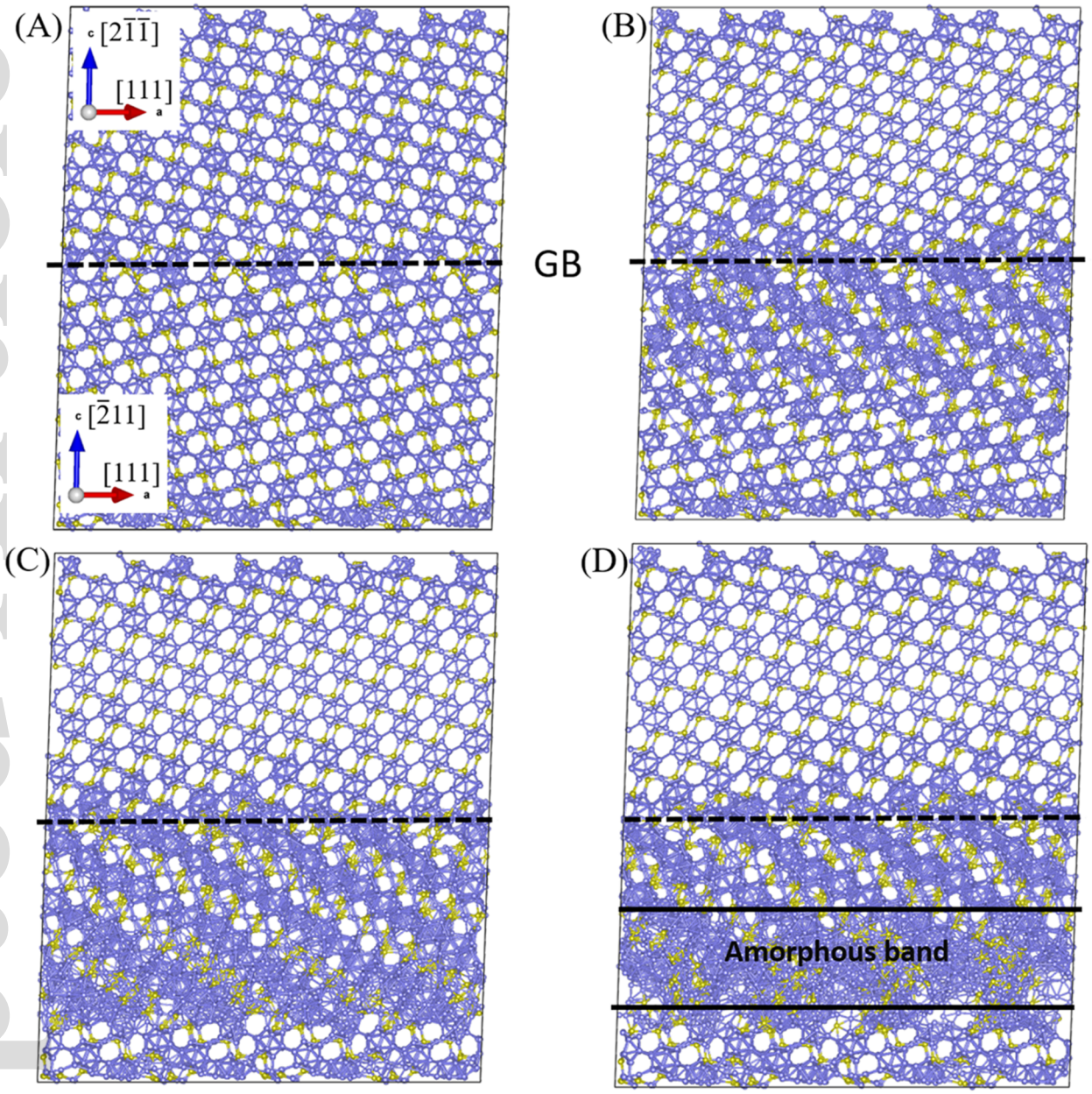

jace_18028_f9.tif

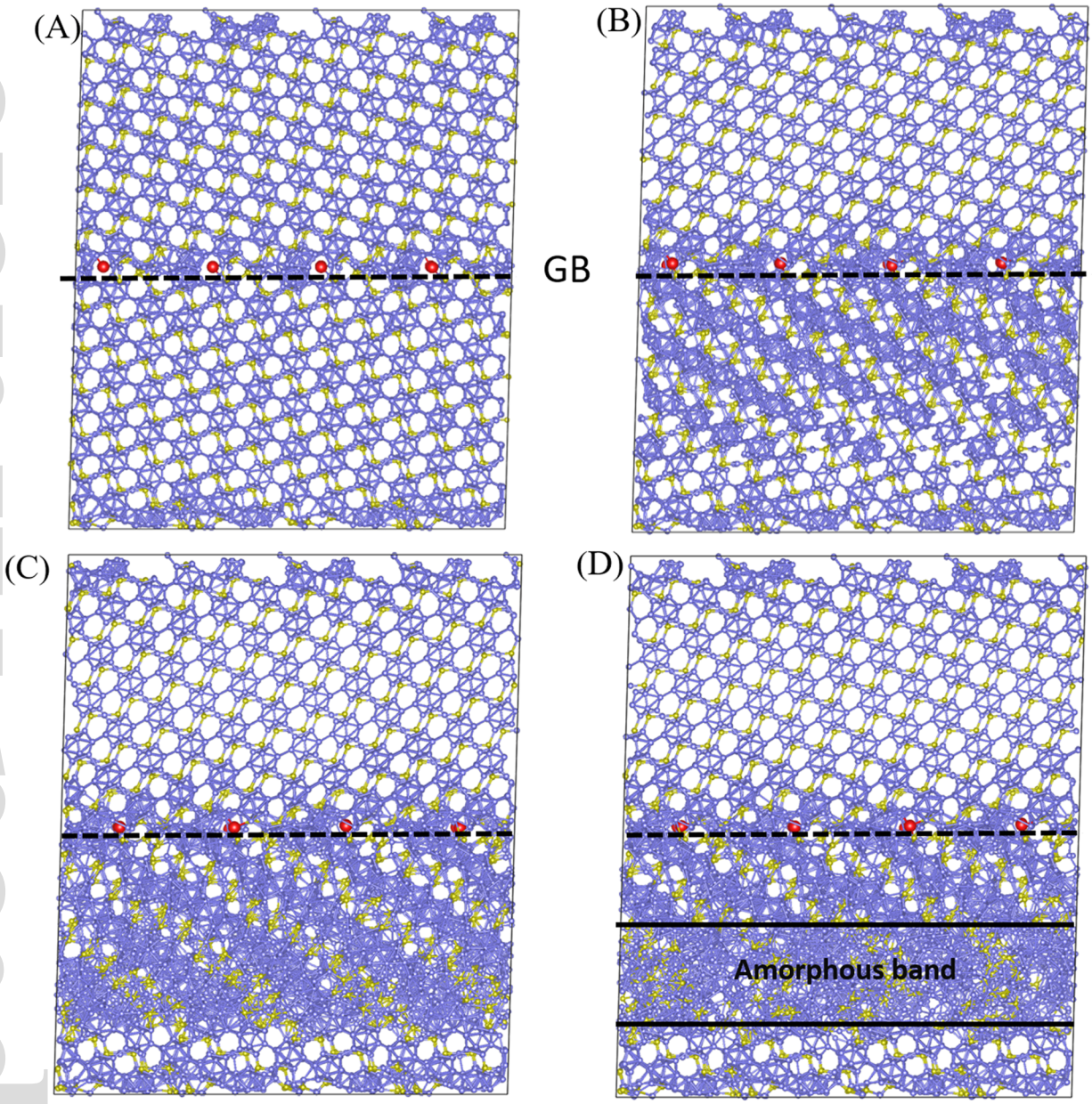

jace_18028_f10.tif